Current Biology, *Volume 23*

Supplemental Information Inventory

Distinct Roles of the Cortical Layers of Area V1 in Figure-Ground Segregation

Matthew W. Self, Timo van Kerkoerle, Hans Supèr, and Pieter R. Roelfsema

Supplemental Figures

Figure S1. Current source density analysis to determine of the depth of the electrode, receptive field size and orientation tuning. (Related to Figure 2)

Figure S2. MUA data from individual animals and t-statistics. (Related to Figure 4)

Figure S3. Example CSD profiles showing the edge-related sink/source pair in upper layer 4 and superfical layers and the average from each animal. (Related to Figure 5)

Figure S4. Latency of the CSD modulation. (Related to Figure 6).

Figure S5. Details of the number of recording sites.

Supplemental Data

*Orientation analysis:*Analysis showing that FGM does not depend on orientation tuning.

Eye movement analysis: Description and results of a control analysis to determine whether the differences in activity between layers were due to variations in the position of the eyes.

Supplemental Experimental Procedures

Stimuli and task

Aligning penetrations based on CSD analysis

Receptive-field measurement

Multi-unit envelope

MUA Statistics

Latency analysis

Number of penetrations and exclusion criteria

Cluster statistics

Supplemental References

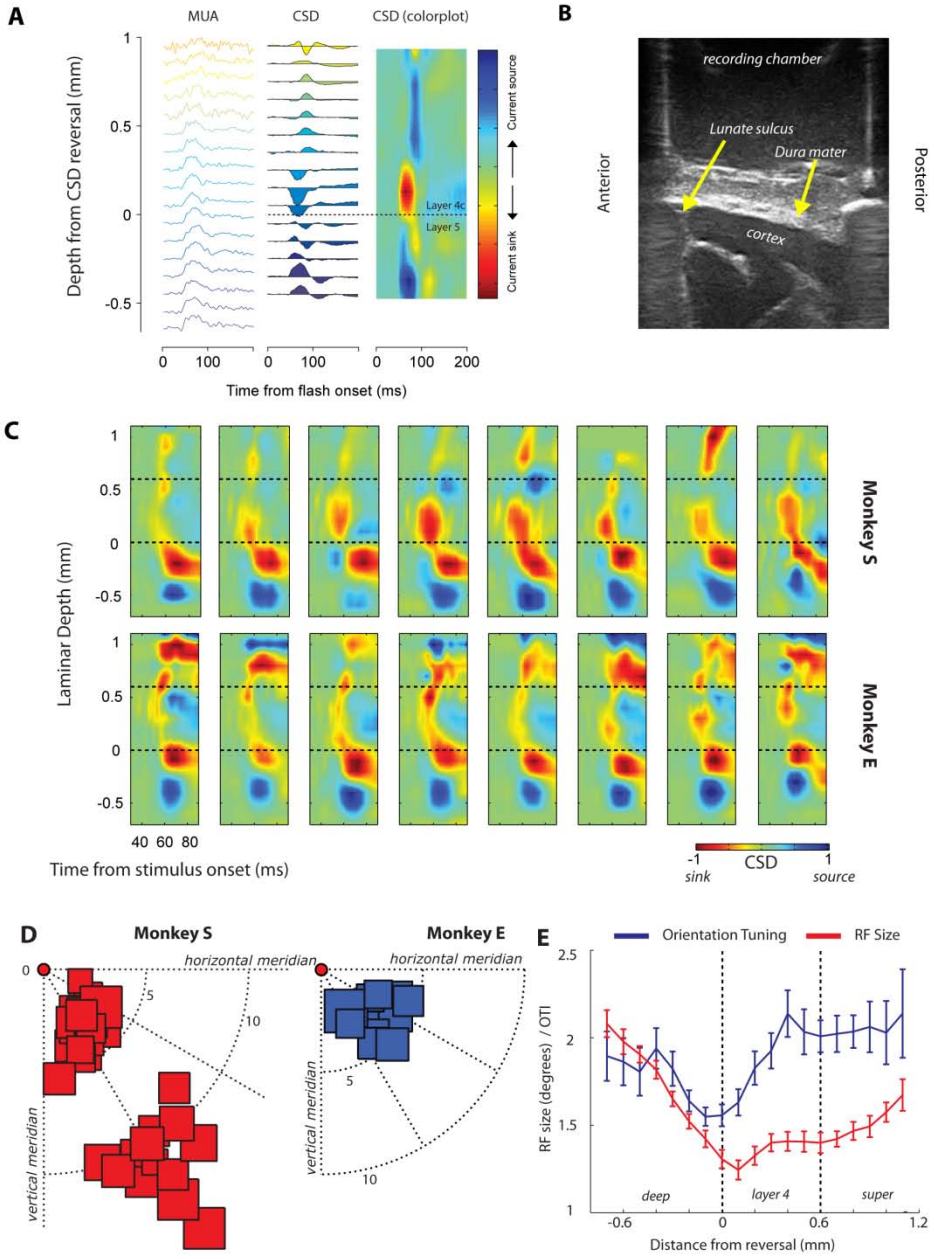

Figure S1. Related to Figure 2. (A) An example penetration showing the MUA (left graph) and CSD (middle and right graph) triggered by the sudden appearance of a full-screen, full-contrast checkerboard stimulus. Simultaneous responses from 17 contacts are shown stacked (the other contacts were excluded due to low signal to noise ratio). In the leftmost columns blue colors indicate deeper channels and green/yellow colors indicate shallow channels. In the rightmost column the red colors show current sinks and the blue colors current sources. The CSD shows a reversal from a current source in the deep layers to a current sink in layer 4c, the boundary is marked by the dashed

line. (B) An ultrasound image taken through the recording chamber showing the operculum of V1. The lunate sulcus is visible at the anterior side of the image and all penetrations were targeted posterior to the lunate. The cortical surface is relatively flat here allowing penetrations orthogonal to the cortical layers. This is important for achieving accurate current source density profiles. (C) Example current-source density profiles from 8 penetrations in monkey S (top row) and monkey E (bottom row). These profiles show the CSD pattern produced by the onset of the full-screen texture (catch-trial condition). (D) Location of RFs from monkey S (red, left graph) from opercular (central RFs) and calcarine V1 recordings (eccentric RFs) and monkey E (blue, right graph) from recordings in the operculum. (E) The average RF size (square-root of the RF area, red line) and orientation tuning index (OTI) as a function of cortical depth. Lower OTIs indicate weaker orientation tuning.

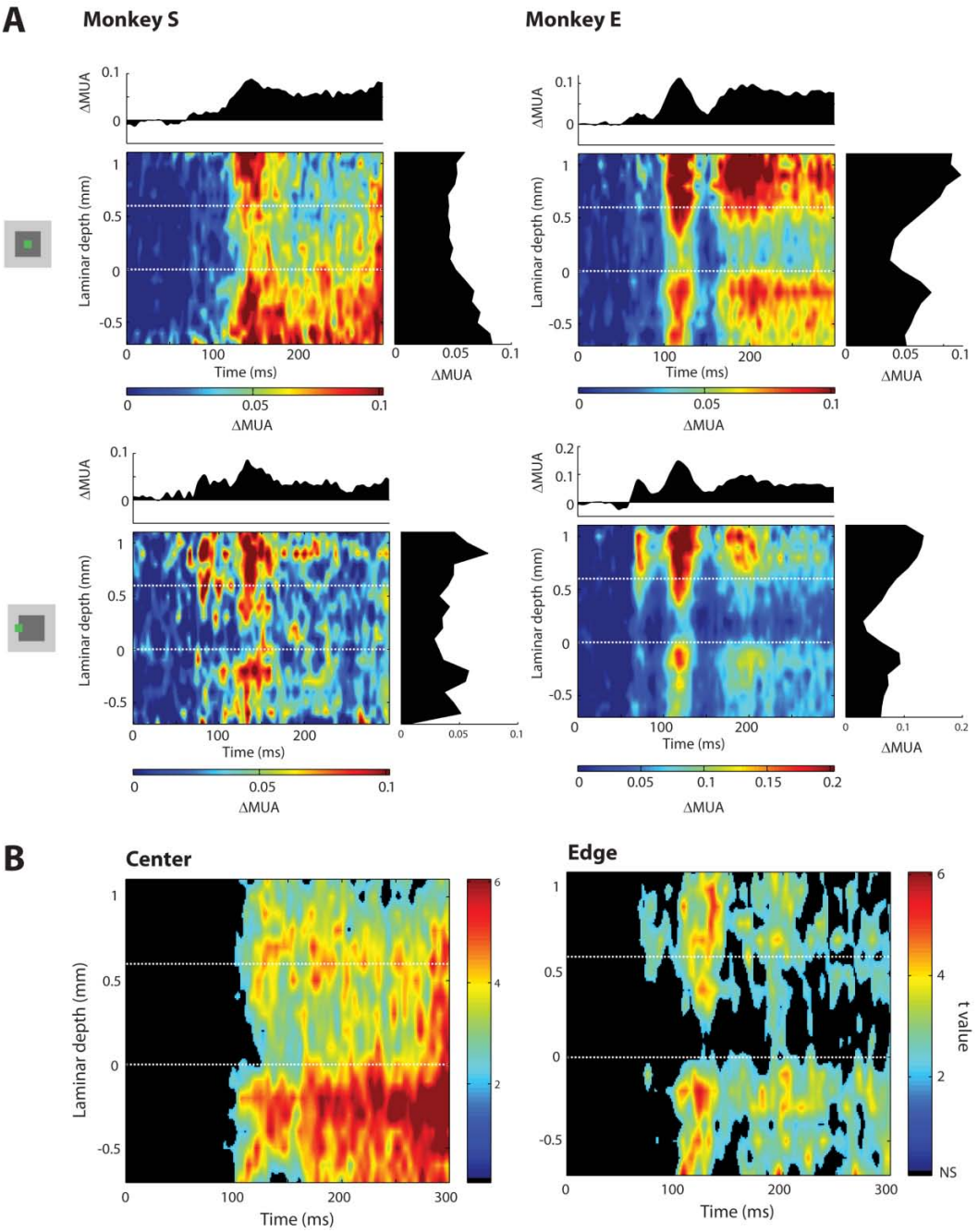

Figure S2. Related to Figure 4. (A) MUA data from the individual animals in the same format as Figure 4A,B. Both the temporal and laminar patterns of FGM were similar. One difference was a lower level of FGM in the superficial layers of Monkey S in a later phase (>200ms), although it was similar to the FGM in Monkey E in an earlier phase (100-200ms). (B) Statistical maps showing t-values from sample-by-sample t-tests between the figure and ground conditions from the centre (left) and edge (right) positions. Non-significant tests ($p < 0.05$, NS) are colored black.

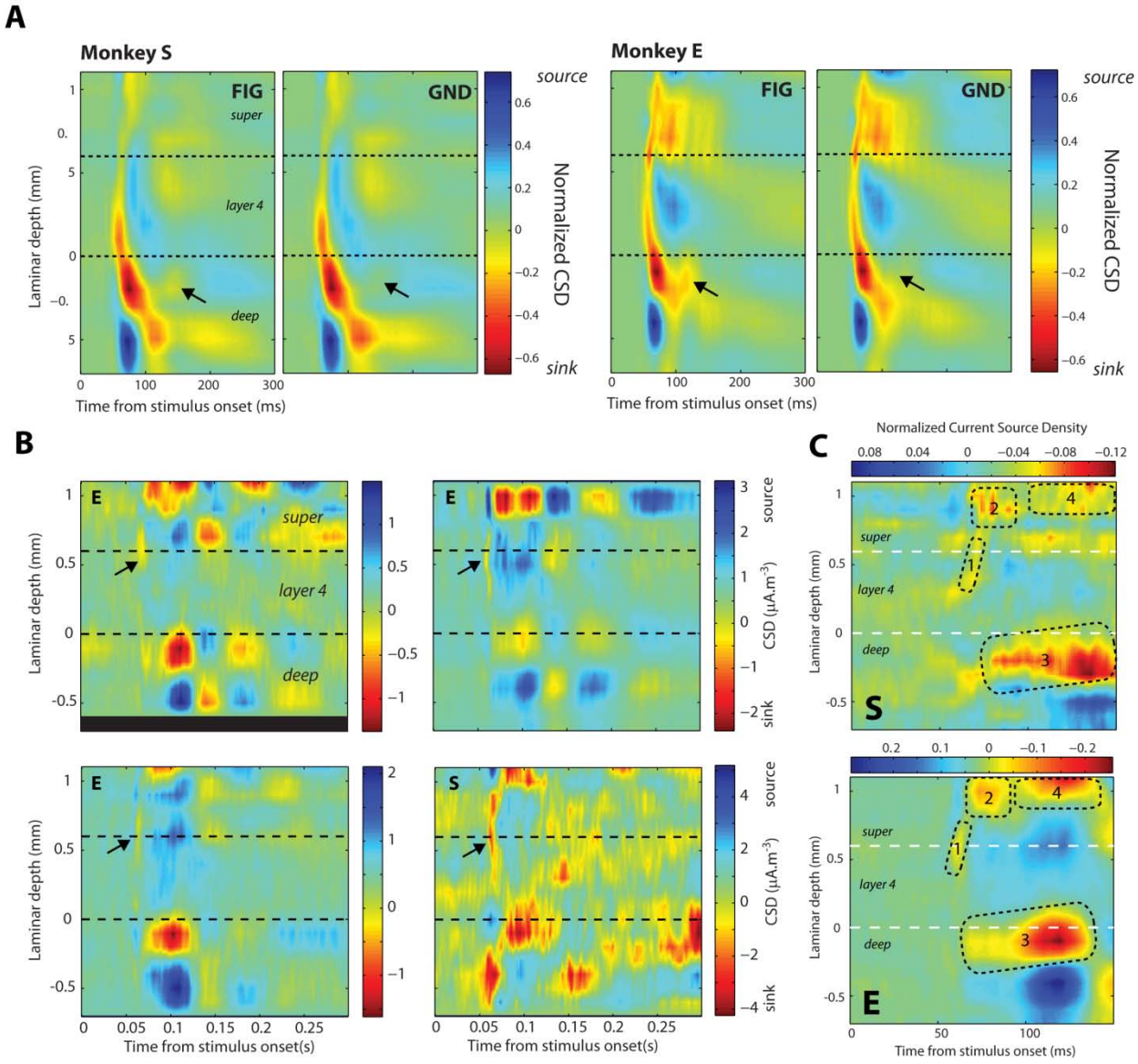

Figure S3. Related to Figure 5. (A) The average normalized CSD patterns from monkey S (left graphs) and monkey E (right graphs) in the figure center and ground conditions individually. The location of the modulatory current sink in layer 5 is indicated by the arrow. This modulatory current arrives at a time-point where there is no obvious net current flow in the ground condition. (B) Example penetrations showing the CSD difference between the response evoked by the figure edge and the background. Conventions are as in Figure 5B. These examples demonstrate the consistency of the extra sink in upper layer 4/superficial layers (black arrow) caused by the presence of the edge in the RF. E/S indicates the monkey. (C) Average data from the individual monkeys showing the CSD difference between the response evoked by the figure edge and the background. Four additional sinks

in the edge condition (labeled 1-4) are identified. Note the similar timing and laminar position in both monkeys.

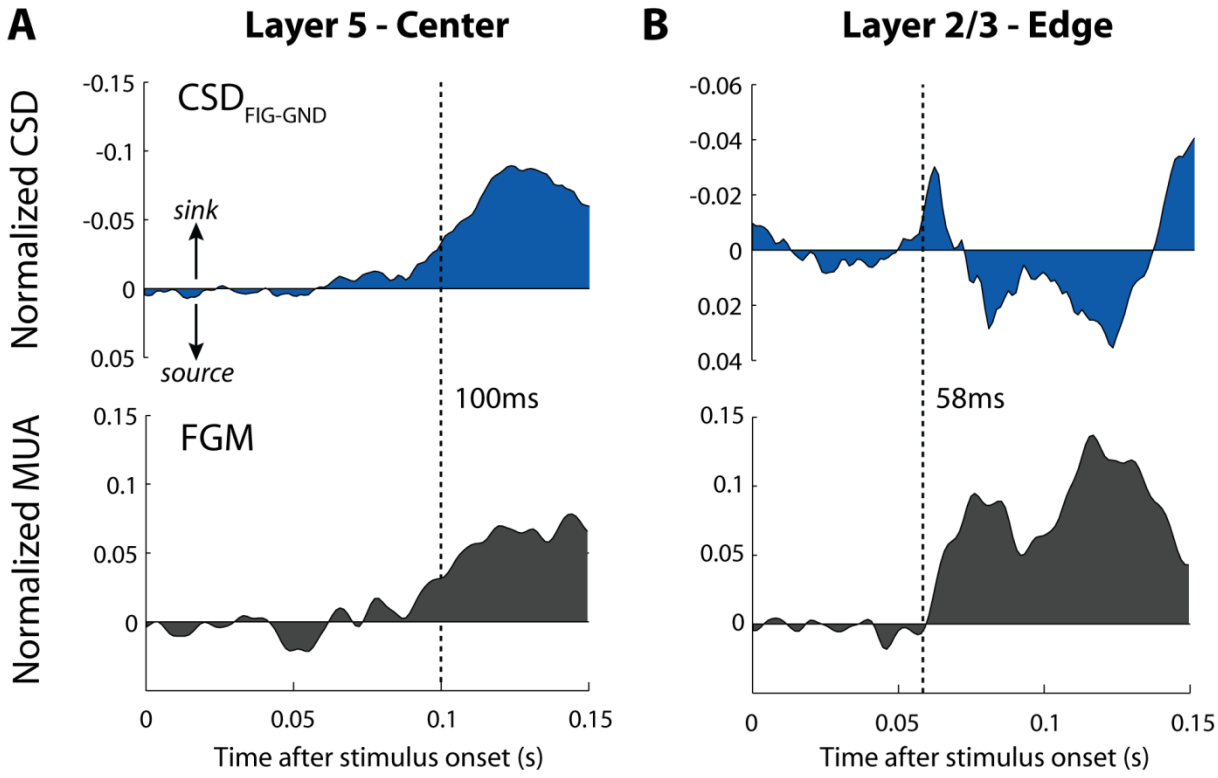

Figure S4. Related to Figure 6. (A) The top graph shows the difference in the CSD between the figure and ground conditions in layer 5 in the center condition (the average of the two electrode sites immediately below layer 4c were used, i.e. -0.1 and -0.2mm). The dashed line shows the latency of the CSD modulation (100ms) which was estimated by taking the point at which the trace reached 33% of the maximum response (it is not necessary to fit the CSD trace with a curve to estimate latency as it is already a low-passed signal). We also calculated the latency of the CSD modulation in layer 1, which was very similar to that of layer 5 (102.3ms). The lower graph shows the level of FGM from the same laminar depth with the CSD latency overlaid. (B) The same format as in (A) but now showing the early edge-related modulation in the superficial layers (depths 0.6 and 0.7mm were averaged). The latency of the CSD sink (58ms) was estimated in the same way as in (A).

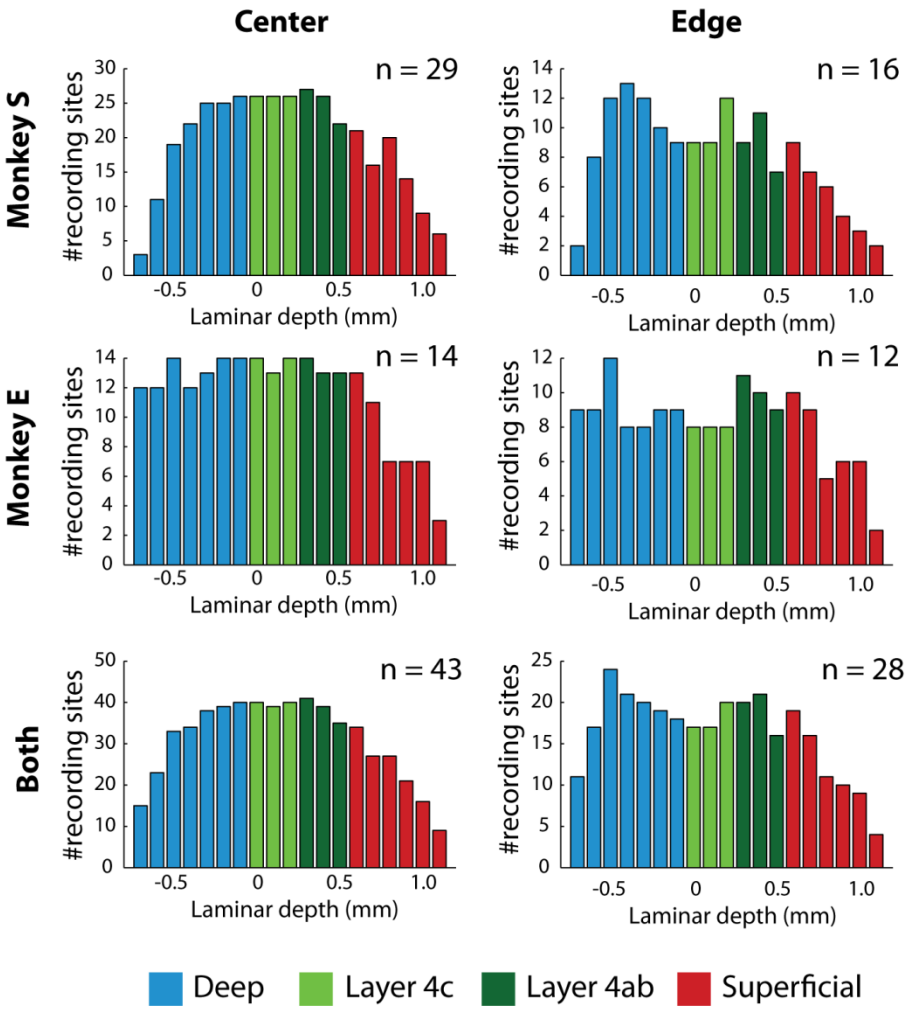

Figure S5. The number of recording sites included in the analysis per layer. The color of the bars indicates the laminar compartment that the electrode site was assigned to. The *n* values indicate the number of penetrations in each data set.

Supplemental Data

Influence of orientation tuning on FGM

We examined whether FGM depended on the neurons' orientation tuning. We first calculated an orientation index based upon the response of the multi-units to the texture stimuli (OTI):

$$OTI = \frac{CTH_{45} - CTH_{135}}{CTH_{45} + CTH_{135}}$$

Where CTH_{45} was the average MUA response during the catch trial condition (0-300ms) with a 45° texture and CTH_{135} was the response to the 135° texture. We considered a multi-unit recording site to be tuned to orientation if this index was greater than 0.1 (prefers 45°) or less than -0.1 (prefers 135°). We then examined how these recording sites responded to figure and ground textures which either matched the preferred orientation of the cell or not. We carried out a 2x2 repeated measures ANOVA with factors context (figure or ground) and orientation of the texture in the RF (preferred or non-preferred). As expected, we found significant main-effects of context and orientation (Orientation: $F_{1,1045} = 1463$, $p<10^{-6}$. Context: $F_{1,1045}=2640$, $p<10^{-6}$), however these two factors did not interact ($F_{1,1045} = 2.12$, $p = 0.15$). We also examined if FGM depended on the strength of the orientation-tuning by correlating the OTI with FGM-strength, but we found no significant correlation ($r^2 = 0.0005$, $p > 0.5$). Thus, the strength of FGM does not depend strongly on the orientation tuning of the recording sites.

Eye movement analysis

During this experiment the animals fixated on a fixation dot of 0.3° in diameter inside a circular window of 1° diameter. We performed an analysis to control for possible differences

in fixational eye-position within this window between the figure and ground conditions. We performed a stratification analysis as described previously [S1]. For each penetration we binned the mean horizontal and vertical eye positions from each trial (bin size 0.25^{o} x 0.25^{o}). We equated the number of trials in each bin across conditions (figure and ground) by randomly removing surplus trials in one of the conditions, thus ensuring that the eye-position distribution was similar across the different conditions. We then reanalyzed the data using the remaining trials. After stratification we still found significant differences in FGM in the centre condition across layer compartments ($F_{3,81.3} = 6.5$, $p = 0.001$). FGM was weakest in layer 4c (FGM in superficial layers and deep layers was significantly stronger than in layer 4c, post-hoc test, both $p < 0.01$, Bonferroni corrected). After stratification, we also replicated the laminar profile of FGM if the RF fell on the edge, with significant differences between the layer compartments (window from 50-100ms, $F_{3,66.4}= 4.5$, $p = 0.006$) . Thus, the laminar differences between the centre and edge FGM were not caused by variations in eye-position.

Supplemental Experimental Procedures

Stimuli and task

After 300ms of fixation, we presented a figure-ground stimulus that was comprised of an oriented texture with a square figure (4^ox4^o) of the orthogonal orientation (Figure 1A). The textures consisted of randomly placed black line elements (45^o or 135^o) on a white background. We made four different textures for each recording session (two of each orientation) and these were presented in a counter-balanced order to ensure that precisely the same line-elements were present in the RF for each condition. After another 300ms, the fixation dot was extinguished and the monkeys were rewarded for making an eye movement to the figure. There were three possible figure locations. One was centered on the neurons' RF (figure condition) and the other two were at an angle of 120^o (ground conditions, Figure 1E). Twenty-five percent of trials were catch-trials without a figure and on these trials the monkey was rewarded for maintaining fixation. Within a block of trials (between 200-500 correct trials) the figure was always presented at the same eccentricity. In different blocks we varied the eccentricity of the figure to create the 'Center' and 'Edge' conditions (Figure 1D).

Aligning penetrations based on CSD analysis

To align different penetrations in depth we used current source density (CSD) analysis. A full-screen, full-contrast checkerboard was presented (duration 250ms, check size 0.3°) while the monkey fixated. The sudden appearance of the checkerboard produced a characteristic and highly repeatable laminar CSD pattern (Fig. S1A,C) with a clear reversal from current sources in the deep layers to a current sink in layer 4c. We identified this reversal point online for each penetration and placed the electrode so that the reversal was as close as possible to

the 8th contact from the tip to ensure coverage of all cortical laminae. We also used this reversal point to align all our recordings in depth at the data analysis stage. Taking one penetration as a reference, we used an automated procedure to shift the other penetrations to minimize the sum-of-squares errors between the CSD of the reference and target penetration between 50 and 100ms after stimulus onset (as this time period gives the most reliable CSD profiles).

Receptive-field measurement

We measured the extent of the multi-unit receptive-field (RF) by determining the onset and offset of the response at each recording site evoked by a moving bar. The RF dimensions were measured precisely by sweeping the bar in the four cardinal directions while the monkey maintained fixation. We measured the average response to a minimum of eight repeats of each direction, and fitted a Gaussian curve to the responses (adjusting mean and standard deviation). The onset and offset of the response were taken as two standard deviations on either side of the mean. The RF border was taken to be the average between the onset position of one direction averaged with the offset position from the opposite direction, a procedure which automatically compensates for the delay between the stimulus and the onset of the neural response [S2]. The RF size varied with laminar compartment (Fig. S1E) (Mixed model, $F_{3,118.7}= 46.2$, $p < 0.001$). The smallest RFs were found in layer 4c in accordance with some [S3,S4] but not all [S5,S6] previous studies, whereas the RFs in the deepest layers were particularly large, as has been reported previously [S5].

Orientation tuning indices (OTIs) were calculated as the ratio between the average response to the preferred orientation of the moving light bar and the response to the least-preferred orientation. The strength of orientation tuning of the multi-unit activity also varied

significantly across the cortical layers (Fig. S1E) (Mixed model, $F_{3,120.1} = 8.9$, $p < 0.001$) being weakest in layer 4c, as has been reported previously for single units [S4,S6-9].

Multi-unit envelope

To study spiking activity we used a multi-unit recording technique that was introduced by Legatt et al. [S10], and was used in several studies from other labs [S11,S12]. The method measures the spiking of neurons in the vicinity of the electrodes as the amplitude of the envelope of the multi-unit signal (MUA) [S2]. The signal from the electrode is first filtered between 500Hz and 5kHz to extract high-frequency (spiking) activity, rectified (negative values become positive) and low-pass filtered at 200Hz to produce MUA. MUA provides an instantaneous measure of the number and amplitude of spikes in the vicinity of the electrode and its measurement does not require the setting of an (arbitrary) spike-detection threshold. We have previously compared responses obtained using MUA with both thresholded multi-unit data and single-unit data and found the responses to be very similar [S2,S13]. Furthermore, we observed that the MUA signal contains contributions from spiking neurons within ~150µm of the contact point [S13], which corresponds to the distance over which the same V1 cell can be recorded with single-unit recording [S14,S15]. The limited distance over which cells are recorded with MUA is supported by the well-localized receptive fields with a size corresponding to the composite receptive field of a few V1 single units (Figure S1D).

MUA Statistics

Statistics assessing the level of FGM for the example penetrations were generated using the average activity on each trial from a laminar compartment as the dependent variable. These values were entered into a two-way independent ANOVA with the factors being condition (figure, ground) and compartment (deep, layer 4c, layer 4ab, superficial).

We carried out our population statistics at the level of laminar compartments. Specifically, data from individual recording sites within a laminar compartment of the same penetration were first averaged and these averages entered into the statistical tests. We corrected for the fact that data from electrode sites from the same penetration are correlated (i.e. not independent) with a hierarchical mixed linear regression model (referred to as a 'mixed model' in the text) with one fixed effect (laminar compartment, 4 levels) and one random effect (penetration). The model contained an intercept term for the random effect and was fit using restricted maximum likelihood in SPSS (IBM, vs. 20). This approach produces identical results to a standard repeated-measures ANOVA if there is no missing data. However, in some penetrations there were insufficient numbers of electrode sites passing our exclusion criteria (or in the case of latency analyses, insufficient sites generating a measurable latency) to generate a compartment average. In these cases the mixed model approach is more powerful. The same mixed model approach was used for testing figure-ground modulation, visual latency, latency of modulation and the level of sustained activity. For *post-hoc* testing a 95% confidence interval was constructed around the estimated marginal means and the Bonferroni correction for multiple comparisons was applied.

Latency Analysis

Our method to calculate the latency of the visual response was based on a previously described method [S16]. The latency of both the visual response and FGM were calculated by fitting a function to the data. We fitted the visual response, *y*, at each time-point, *t*, with the sum of two Gaussians and a cumulative Gaussian using non-linear least-squares fitting (MATLAB, Mathworks Inc.):

$$y(t) = \frac{G_1 e^{-0.5\left(\frac{t-\mu_1}{\sigma_1}\right)^2}}{\sqrt{2\pi}\sigma_1} + \frac{G_2 e^{-0.5\left(\frac{t-\mu_2}{\sigma_2}\right)^2}}{\sqrt{2\pi}\sigma_2} + 0.5G_3\left[1 + erf\left(\frac{t-\mu_3}{\sqrt{2{\sigma_3}^2}}\right)\right]$$

Free parameters of the fit are the amplitudes (G_{1-3}), means (μ_{1-3}) and standard deviations (σ_{1-3}) of the Gaussians, and *erf* stands for the error function.

To calculate the latency of FGM we fitted the same function to the difference between the responses evoked by the figure and the background, separately for every layer compartment. The method resulted in good fits of both the visual response (median adjusted $r^2 = 0.94$) and FGM (median adjusted $r^2 = 0.73$). We (arbitrarily) defined the latency as the time point at which the fitted curve reached 33% of the maximum of the earliest Gaussian.

An important advantage of this technique is that the latency does not strongly depend on the signal-to-noise ratio of the response or the number of trials (in contrast, latency measurements based on the first of a number of significant time bins tend to yield shorter latencies when more data has been acquired). Moreover, we could use the same curve to fit the visually driven response, the centre FGM and the edge FGM so that these latencies could be directly compared.

Number of penetrations and exclusion criteria

We recorded from a total of 43 penetrations in which we acquired data from the center position (29 from monkey S and 14 from monkey E) yielding a total of 590 recording sites (370 in monkey S and 220 in monkey E) after applying our exclusion criteria (See below). We also recorded data from the edge of the figure in 16 penetrations in monkey S (154 recording sites) and 12 penetrations in monkey E (156 sites). For all of the penetrations in which we recorded data from the edge condition we also recorded data from the center condition, with the exception of one penetration in which we only recorded edge data yielding 27 matched penetrations for the center and edge data. We included eight penetrations from Monkey S with a laminar probe containing a fluid-line for the injections of drugs. The effects of the drug

injections were reported elsewhere [S13], whereas the data included here came from the pre-injection period. The number of included of recording sites per layer per condition per monkey is reported in Figure S5.

We removed recording sites with a signal-to-noise ratio (SNR) of less than 1. SNR was calculated as the difference between the evoked visual response (in a window from 0-300ms) and the spontaneous activity during the pre-stimulus period (-150-0ms) normalized to the standard deviation across trials of activity in the pre-stimulus period. We also removed recordings sites for which the RF was not well defined or if the RF was larger than 2.5^{o}. For the analysis of FGM in the center of the figure we did not evaluate activity at recording sites where the RF edge came within 0.2^{o} of the figure edge. For the analysis of edge FGM, we only included recording sites with an RF which included the figure edge. The exclusion criteria together (too high/low cortical depth, low signal-to-noise ratio, RF too large, not well defined or at wrong location) resulted in the exclusion of 41.3% of all potential MUA-recording sites, but the CSD at these sites could generally be used.

CSD cluster statistics

The statistical analysis of the significance of differences in the CSD between figure and background was based on a non-parametric cluster analysis [S17]. First, we calculated *t*-scores for the difference in the CSD evoked by the figure and the background across penetrations for each time-sample/depth pair, thus producing a 2-dimensional array of *t*-scores (time-samples x depth). The *t*-map was thresholded, setting non-significant *t*-values ($p < 0.05$) to zero (Figure 5C,D). We clustered adjacent *t*-scores with the same sign and calculated a cluster statistic; the sum of the absolute *t*-scores per cluster. To determine the significance of these clusters, we carried out a bootstrapping analysis. We randomly shuffled the data (mixing trials from the figure and ground condition) to produce 1000 CSD difference maps (see below

for details) and subjected them to the same procedures as the real data. We took the maximum of the sum of the *t*-values in each cluster as the bootstrap statistic and generated a shuffled distribution of this statistic. We then compared the calculated *t*-values from each cluster of the actual data to the shuffled distribution. Clusters were considered significant if their absolute *t*-value fell above the 95th percentile of the shuffled distribution. We also applied a size-threshold, excluding clusters that were smaller than 10 time-sample/depth pairs. The advantage of this statistic is that it uses both the magnitude of the *t*-scores within a cluster and also the size of the cluster so that is sensitive to strong sinks and sources and also to weak, but spatially extended, sinks and sources.

The bootstrapping procedure was as follows:

1) For each electrode site of a penetration, the LFP from the figure and ground trials were collected and placed into one large distribution, with one entry per trial.

2) Two reshuffled conditions ($Figure_r$ and $Ground_r$) were created for every penetration by sampling (with replacement) from this pooled distribution of trials. The same number of trials per condition were drawn as were present in the original data set. The average LFP for each condition was then calculated from the reshuffled trials and stored for each electrode site in the penetration.

3) The LFP maps were converted into CSD-profiles using the equation described in the Experimental Procedures. The resulting CSD maps were converted into a CSD difference map by subtracting the CSD map of the simulated ground condition from that of the simulated figure condition.

4) Steps 1-3 were repeated for each penetration and the CSD difference maps of different penetrations were aligned in depth.

5) One-sample t-tests were performed for each time/depth sample (229 time-samples [0-300ms] x 19 depths). The resulting t-maps were thresholded and non-significant ($p < 0.05$) samples were set to zero.

6) The thresholded t-maps were clustered. Negative and positive t-scores were separately clustered and a cluster-statistic, the sum of the absolute t-values in the cluster, was calculated for each cluster. The maximum of the summed cluster values was then taken as the bootstrap statistic.

7) Steps 1-6 were repeated 1000 times to produce a distribution of cluster statistics.

8) The actual cluster statistics from the original data were compared to the cluster-distribution.

Supplemental Reference List

[S1] Roelfsema P.R., Lamme V.A., and Spekreijse H. (1998). Object-based attention in the primary visual cortex of the macaque monkey**.** Nature *395***,** 376-381.

[S2] Supèr H. and Roelfsema P.R. (2005). Chronic multiunit recordings in behaving animals: advantages and limitations**.** Prog. Brain Res. *147***,** 263-282.

[S3] Schiller P.H., Finlay B.L., and Volman S.F. (1976). Quantitative studies of single-cell properties in monkey striate cortex. II. Orientation specificity and ocular dominance**.** J. Neurophysiol. *39***,** 1320-1333.

[S4] Hubel D.H. and Wiesel T.N. (1977). Ferrier lecture. Functional architecture of macaque monkey visual cortex**.** Proc. R. Soc. Lond B Biol. Sci. *198***,** 1-59.

[S5] Sceniak M.P., Hawken M.J., and Shapley R. (2001). Visual spatial characterization of macaque V1 neurons**.** J. Neurophysiol. *85***,** 1873-1887.

[S6] Snodderly D.M. and Gur M. (1995). Organization of striate cortex of alert, trained monkeys (Macaca fascicularis): ongoing activity, stimulus selectivity, and widths of receptive field activating regions**.** J. Neurophysiol. *74***,** 2100-2125.

[S7] Ringach D.L., Shapley R.M., and Hawken M.J. (2002). Orientation selectivity in macaque V1: diversity and laminar dependence**.** J. Neurosci. *22***,** 5639-5651.

[S8] Gur M., Kagan I., and Snodderly D.M. (2005). Orientation and direction selectivity of neurons in V1 of alert monkeys: functional relationships and laminar distributions**.** Cereb. Cortex *15***,** 1207-1221.

[S9] Blasdel G.G. and Fitzpatrick D. (1984). Physiological organization of layer 4 in macaque striate cortex**.** J. Neurosci. *4***,** 880-895.

[S10] Legatt A.D., Arezzo J., and Vaughan H.G., Jr. (1980). Averaged multiple unit activity as an estimate of phasic changes in local neuronal activity: effects of volume-conducted potentials**.** J. Neurosci. Methods *2***,** 203-217.

[S11] Logothetis N.K., Pauls J., Augath M., Trinath T., and Oeltermann A. (2001). Neurophysiological investigation of the basis of the fMRI signal**.** Nature *412***,** 150-157.

[S12] Xing D., Yeh C.I., and Shapley R.M. (2009). Spatial spread of the local field potential and its laminar variation in visual cortex**.** J. Neurosci. *29***,** 11540-11549.

[S13] Self M.W., Kooijmans R.N., Super H., Lamme V.A., and Roelfsema P.R. (2012). Different glutamate receptors convey feedforward and recurrent processing in macaque V1**.** Proc. Natl. Acad. Sci. U. S. A *109***,** 11031-11036.

[S14] Henze D.A., Borhegyi Z., Csicsvari J., Mamiya A., Harris K.D., and Buzsaki G. (2000). Intracellular features predicted by extracellular recordings in the hippocampus in vivo**.** J. Neurophysiol. *84***,** 390-400.

[S15] Gray C.M., Maldonado P.E., Wilson M., and McNaughton B. (1995). Tetrodes markedly improve the reliability and yield of multiple single-unit isolation from multi-unit recordings in cat striate cortex**.** J. Neurosci. Methods *63***,** 43-54.

[S16] Roelfsema P.R., Tolboom M., and Khayat P.S. (2007). Different processing phases for features, figures, and selective attention in the primary visual cortex**.** Neuron *56***,** 785-792.

[S17] Maris E. and Oostenveld R. (2007). Nonparametric statistical testing of EEG- and MEG-data**.** J. Neurosci. Methods *164***,** 177-190.